Cavitation caused by an elastic membrane deforming under the jetting of a spark-induced bubble

Yuxue Zhong
Key Laboratory for Mechanics in Fluid Solid Coupling Systems, Institute of Mechanics, Chinese Academy of Sciences, Beijing 100190, China and School of Engineering Science, University of Chinese Academy of Sciences, Beijing 100049, China

Jingzhu Wang*
Key Laboratory for Mechanics in Fluid Solid Coupling Systems, Institute of Mechanics, Chinese Academy of Sciences, Beijing 100190, China; School of Engineering Science, University of Chinese Academy of Sciences, Beijing 100049, China; and Guangdong Aerospace Research Academy, Guangzhou 511458, China

Jianlin Huang
Key Laboratory for Mechanics in Fluid Solid Coupling Systems, Institute of Mechanics, Chinese Academy of Sciences, Beijing 100190, China and School of Future Technology, University of Chinese Academy of Sciences, Beijing 100049, China

Yiwei Wang
Key Laboratory for Mechanics in Fluid Solid Coupling Systems, Institute of Mechanics, Chinese Academy of Sciences, Beijing 100190, China; School of Engineering Science, University of Chinese Academy of Sciences, Beijing 100049, China; and School of Future Technology, University of Chinese Academy of Sciences, Beijing 100049, China

(Received 24 April 2024; accepted 3 September 2024; published 19 September 2024)

The collapse of a spark-induced bubble results in a high-speed jet, and when that jet impacts an elastic membrane, the latter deforms considerably and is accompanied by secondary cavitation. The cavitation bubble then moves away from the membrane with subsequent oscillation. To study the mechanism for this cavitation, experiments involving diffuse light and particle image velocimetry were conducted to capture the behaviors of the cavitation bubble and flow field resulting from the rapid deformation of the membrane. Analyzing the velocity and pressure fields reveals secondary cavitation induced by a sudden acceleration rather than a large velocity. Secondary cavitation occurs when the dimensionless inertial force overcomes the dimensionless pressure difference required for cavitation; subjecting these dimensionless quantities to a parametric study shows that the secondary cavitation occurs when the former is greater than the latter. During the collapse of the cavitation bubble, a thin jet points toward the membrane with an impact velocity of approximately 35 m/s. The subsequent oscillation of the cavitation bubble results in vortex flow moving away from the membrane. These findings provide insights into engineering applications such as bioengineering and mixing.

DOI: 10.1103/PhysRevFluids.9.093604

*Contact author: wangjingzhu@imech.ac.cn

I. INTRODUCTION

Interactions between oscillating bubbles and elastic boundaries are crucial in many biomedical applications, such as ultrasound treatments [1], laser treatments [2], and shock-wave lithotripsy [3]. In these applications, nonspherical oscillating bubbles are generated near compliant tissue layers, whereupon the jetting of the bubbles causes tissue damage. Therefore, understanding these interactions is important for optimizing therapy and minimizing associated injuries.

The interactions of oscillating bubbles with elastic boundaries have attracted much attention in recent years [3–9]. Near an elastic boundary, a bubble subjected to counteracting forces and the Bjerknes attraction force induced by the elastic boundary exhibits complex dynamics. The bubble may assume a mushroom shape and split into two daughter bubbles [10], with two jets directed away from and toward the boundary [11–13], a behavior that generally depends on parameters such as the standoff parameter γ and the elastic modulus E for thick boundaries or the thickness d for thin membranes [14,15]. High-velocity jets can penetrate the elastic boundary [16–18] and subject it to intense tensile deformation.

Previous studies have focused mainly on oscillating bubble dynamics and the response of elastic boundaries. However, as shown in Fig. 1(b), our experiments have revealed a previously unreported cavitation phenomenon, termed secondary cavitation. In the experimental setup shown in Fig. 1(a), a spark-induced bubble is generated in the upper flow field above an elastic membrane. When the jet from the collapse of the bubble impacts the membrane, as indicated by the downward white arrow [Fig. 1(b), t_0], the membrane undergoes rapid downward deformation. In the lower flow field, the incipient secondary cavitation bubbles cover the surface of the membrane [Fig. 1(b), $t_0 + 80$ μs]. To highlight the phenomenon, the area where secondary cavitation occurs is enclosed with a red dotted line, and the membrane boundary is depicted with a white dashed line. The incipient secondary bubbles then violently expand and merge into a large cavitation bubble [Fig. 1(b), $t_0 + 650$ μs]. Cavitation can be induced by the reflection of bubble-collapsing shock waves at interfaces [19–24], and

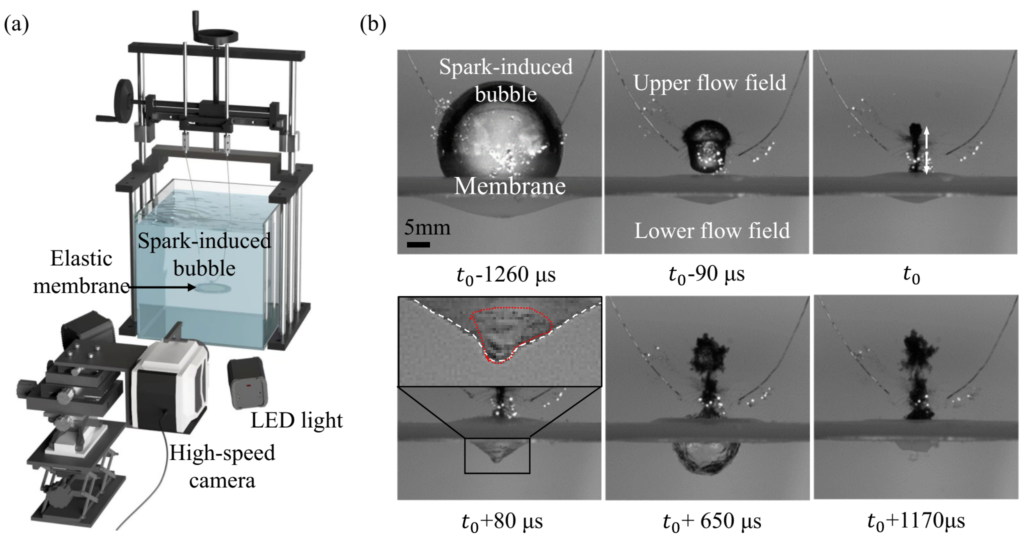

FIG. 1. Setup of diffuse-light experiment for observing the formation of secondary cavitation induced by deformation of the elastic membrane. (a) Schematic of experimental setup. (b) Experimental phenomena for $\gamma = 0.5$ and $d^* = 0.14$, where γ is the dimensionless distance from the spark-induced bubble to the membrane and d^* is the dimensionless stiffness of the membrane. The collapse jet impacts the elastic membrane at time t_0. In the inset for $t_0 + 80$ μs, the red dotted line encloses the area of secondary cavitation, and the white dashed line marks the membrane boundary.

especially at interfaces with large differences in acoustic impedance (e.g., a gas-liquid interface), strong tension can arise. In our work, the acoustic impedance of the membrane is comparable to that of the water, rendering the reflection of shock waves incapable of generating adequate tension. Furthermore, because the water in the experiment had been degassed, acoustic effects are deemed insignificant in the occurrence of secondary cavitation.

In hydrodynamics, there are two general mechanisms for cavitation: (i) high-speed flow and (ii) violent acceleration. In mechanism (i), cavitation occurs when the local static pressure drops rapidly to below the saturated vapor pressure due to an increase in dynamic pressure; this is commonly observed in hydrodynamic vehicles, such as hydrofoils and propellers [25,26], leading to increased drag. Mechanism (ii) occurs because of sudden acceleration of the fluid, whereupon the inertial force surpasses the pressure difference, resulting in cavitation [27,28]; this type of cavitation occurs frequently in hydraulic machinery such as pipelines and turbines [29], often causing catastrophic destruction.

To investigate the mechanism for secondary cavitation, we recorded its dynamics in diffuse light using a high-speed camera and then used particle image velocimetry (PIV) to measure the flow field. This paper is organized as follows. In Sec. II, we detail the experimental setups and method for pressure field reconstruction; the former includes an observation setup for phenomena and a PIV setup for measuring the flow field with secondary cavitation. In Sec. III, we present the experimental phenomena and time-resolved flow fields: first, we compare phenomena with and without the occurrence of secondary cavitation and provide a phase diagram for that occurrence; second, we analyze the characteristics of the velocity and pressure fields for secondary cavitation and investigate its mechanism; third, the regime of secondary cavitation is determined via a parametric study; lastly, we study the subsequent oscillations of the secondary cavitation bubble. Finally, the paper concludes in Sec. IV.

II. EXPERIMENTAL METHODS

To investigate the mechanism of secondary cavitation, we conducted a diffuse-light experiment to observe the phenomenon and a PIV experiment to measure the flow-field information. In Sec. II A, the setup for the diffuse-light experiment is outlined, where we record the dynamics of the interaction between a spark-induced bubble and an elastic membrane, along with the subsequently induced secondary cavitation phenomenon. In Sec. II B, the setup for the PIV experiment is described, where fluorescent particles are used to trace the fluid motion in order to measure the flow field. In Sec. II C, the method for reconstructing the pressure field is introduced.

A. Diffuse-light experiment

The setup for the diffuse-light experiment comprised a water tank, a high-speed camera, and light-emittiing diode (LED) light sources. As shown in Fig. 1(a), the high-speed camera (V2512; Phantom Co., Ltd., USA) recorded the interactions between a spark-induced bubble and an elastic membrane. In the water tank filled with distilled water, single spark-induced bubbles were generated via the discharge of copper wires at a voltage of 300 V. The high-speed camera operated at 100 000 frames per second (fps) with an exposure time of 9.4 μs; its resolution was 6.8 pixels per millimeter, and the field of view was 256 × 256 pixels. Two LED light sources were placed on the same side as the camera for illumination.

The elastic membranes were made from Ecoflex silicone rubber (No. 0030; Smooth-on, Inc.). Equal weights of gels A and B were mixed together and then stirred in a glass beaker, degassed in a vacuum drying chamber, and poured into cylindrical molds. Finally, they were solidified at 25 °C for 4 h. The elastic modulus E of this silicone rubber material was determined using a tensile-strength testing machine with a tensile rate of 20 mm/min; the 100% tensile modulus E of the material was 68.95 kPa. The membrane was fixed around its periphery with no degrees of freedom and could only

TABLE I. Parameters varied in experiments.

Parameter	Definition	Range
Dimensionless standoff distance γ	$\frac{h}{R_{\max}}$	0.10–0.70
Dimensionless membrane stiffness d^*	$\frac{Ed}{\Delta p R_{\max}}$	0.05–0.28

be deformed within a radius of 30 mm from its center. The membrane was positioned horizontally beneath the bubble with their centers aligned.

The experiments involved varying two main parameters as derived via dimensional analysis in Appendix A. The first parameter is the dimensionless standoff distance $\gamma = h/R_{\max}$, defined as the ratio of the initial distance h between the spark-induced bubble and the elastic membrane to the maximum radius of the bubble $R_{\max} = 15$ mm; varying h caused γ to vary in the range 0.10–0.70. The other parameter is the dimensionless elastic membrane stiffness $d^* = Ed/(\Delta p R_{\max})$, where E is the elastic modulus, d is the membrane thickness, and $\Delta p = p_a - p_v$ is the difference between the ambient pressure p_a and the saturated vapor pressure p_v, which was 98.66 kPa at 20 °C. The values of d^* were 0.05, 0.09, 0.14, 0.19, 0.23, and 0.28, corresponding to $d = 1$–6 mm. Table I summarizes the parameters that were varied in the experiments.

B. Flow-field measurement via PIV

The setup for the PIV experiment comprised a water tank, a continuous laser, and a high-speed camera equipped with a high-pass filter. Fluorescent particles (Fluoro-Max 36-2; Thermo Scientific) were used to trace the flow field; these were excited by a laser sheet emitted from below, and their images were captured by the high-speed camera, as shown in Fig. 2. The fluorescent particles

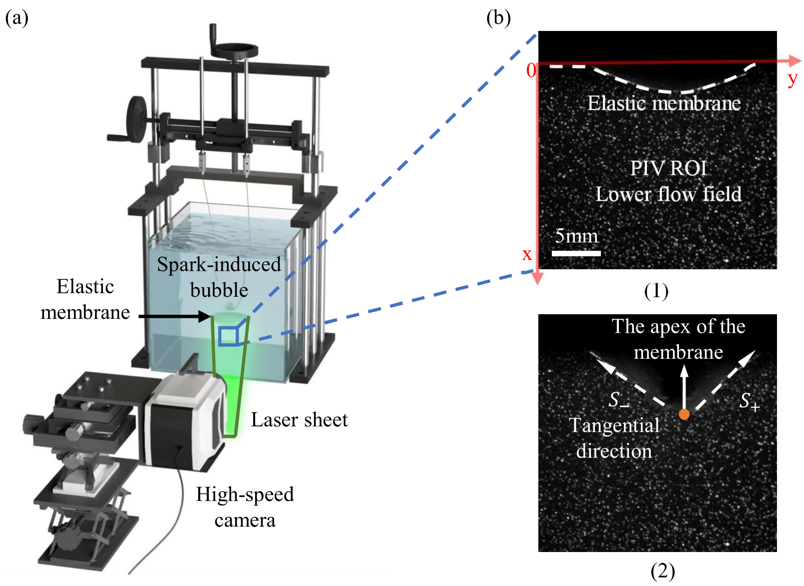

FIG. 2. Setup of the PIV experiment for measuring flow-field information. (a) Schematic of the experimental setup. (b) Particle images at the time of the initial membrane deformation under jet impingement (frame 1) and at the time of occurrence of cavitation (frame 2). In frame 1, the white dashed line represents the elastic membrane. In frame 2, the dashed arrows represent the tangential directions of the membrane, and the orange circle represents its apex.

had a diameter of 6 μm, with a peak excitation wavelength of 542 nm and a peak emission wavelength of 612 nm; these particles were seeded uniformly in the tank. The laser (LWPIV-Super-50 power) was operated in continuous emission mode with a wavelength of 532 nm and an energy of 50 W. The laser plane was perpendicular to the lens and in the same plane as the maximum contour of the elastic membrane. The high-speed camera operated at 150 000 fps with an exposure time of 5 μs; its resolution was 16 pixels per millimeter and the field of view was 256 × 256 pixels.

Figure 2(b) shows recorded particle images of the flow field. In frame 1, the white dashed line indicates the membrane, and from continuity, the flow near the membrane follows the latter's motion. As indicated by the red arrows, the horizontal direction is the y axis and the vertical direction is the x axis. In frame 2, the orange circle marks the apex of the membrane, and the white dashed arrows mark its tangential directions; to the left of the apex is the negative tangential direction S_-, while to the right of the apex is the positive tangential direction S_+. For the PIV experiment, the time corresponding to frame 1 in Fig. 2(b) is the initial time t_0, indicating the collapse jet impacting the membrane, and the time corresponding to frame 2 is when cavitation occurs.

The particle images underwent postprocessing to derive the velocity field, along with uncertainty evaluation. Also, the pressure field was reconstructed from the velocity field. A multipass approach was used to calculate the velocity field. First, two iterations were performed using a 64 × 64 window with 50% overlap for initial estimation, then three iterations were performed using a 16 × 16 window with 75% overlap to obtain the final velocity field. The uncertainty of the PIV vector field was evaluated using correlation statistics [30]. The maximum uncertainty in the velocity field was less than 10%, deemed sufficient for flow-field analysis (see Appendix B for details about the uncertainty evaluation of the PIV flow field). The pressure field was then derived from the flow field in Lagrangian form. The far-field region where the velocity approaches zero served as the reference region with a reference pressure set to zero. The pressure reconstruction method is as follows.

C. Instantaneous planar pressure field

The instantaneous pressure field under unsteady flow conditions is reconstructed using the Lagrangian approach, which involves two steps: (i) the pressure gradient is evaluated by locally applying the momentum equation in Lagrangian form; and (ii) the pressure field is obtained by solving the Poisson equation [31,32].

For unsteady incompressible flow, the instantaneous velocity and acceleration fields are used to calculate the pressure gradient term via the momentum equation:

$$\nabla p = -\rho \frac{D\mathbf{u}}{Dt} + \mu \nabla^2 \mathbf{u}, \tag{1}$$

where p is the pressure, t is time, $\mathbf{u}$ is the velocity vector, and μ is the dynamic viscosity of water. The effect of the viscous term $\mu\nabla^2\mathbf{u}$ on the pressure gradient can generally be neglected. Here, $D\mathbf{u}/Dt$ is the material acceleration, which is the acceleration of a fluid particle followed from a Lagrangian perspective:

$$\frac{D\mathbf{u}}{Dt} = \frac{d\mathbf{u}_p(t)}{dt} = \frac{\mathbf{u}_p(\mathbf{x}_p(t), t)}{dt}, \tag{2}$$

where $\mathbf{x}_p(t)$ and $\mathbf{u}_p(t)$ are the position and velocity of a particle at time t, respectively.

The fluid trajectories were reconstructed using a pseudotracking approach as shown in Fig. 3. For the PIV image at time t, the velocity of the particle at position $\mathbf{x}_p(t)$ is $\mathbf{u}_p(t)$, and the approximate trajectory of the particle (shown by the dashed line in Fig. 3) is reconstructed based on its velocity. To simplify the illustration, a first-order (linear) fluid path is reconstructed, given by

$$\widetilde{\mathbf{x}_p}(t \pm \Delta t) = \mathbf{x}_p(t) \pm \mathbf{u}_p(t)\Delta t. \tag{3}$$

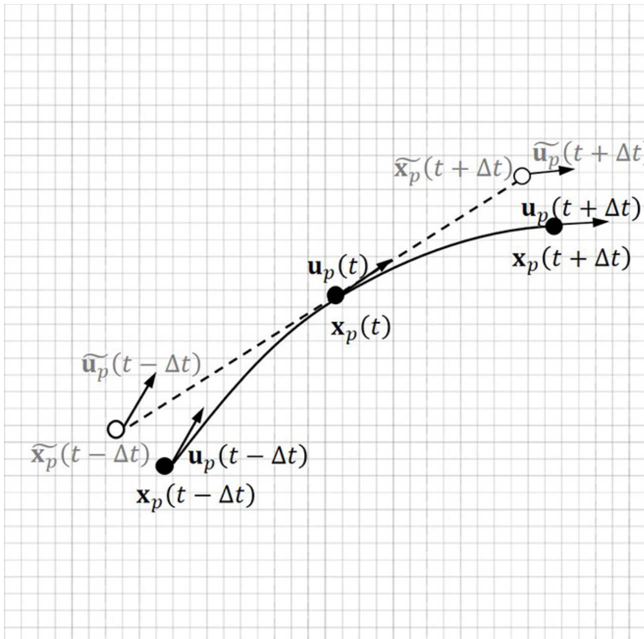

FIG. 3. Illustration of the Lagrangian approach for determining material acceleration. The solid curve represents the actual particle trajectory, with the real particle positions $\mathbf{x}_p$ indicated by the solid circles. The dashed line represents the reconstruction particle trajectory for linear approximation, with the estimated particle positions $\widetilde{\mathbf{x}_p}$ indicated by the empty circles.

The approximate positions of the particle at times $t \pm \Delta t$ (shown as the empty circles in Fig. 3) are deduced as $\widetilde{\mathbf{x}_p}(t \pm \Delta t)$. At times $t \pm \Delta t$, the velocities at positions $\widetilde{\mathbf{x}_p}(t \pm \Delta t)$ are $\widetilde{\mathbf{u}_p}(t \pm \Delta t)$. As shown in Fig. 3, the particle positions (empty circles) determined by the reconstructed particle trajectory (dashed line) differ slightly from the actual particle positions (solid circles) determined by the true particle trajectory (solid line) for a very small time interval Δt.

The material acceleration is obtained by computing the velocity change when following a fluid particle along its reconstructed particle trajectory:

$$\frac{D\mathbf{u}}{Dt}(\mathbf{x}_p(t), t) = \frac{\widetilde{\mathbf{u}_p}(t+\Delta t) - \widetilde{\mathbf{u}_p}(t-\Delta t)}{2\Delta t}. \tag{4}$$

To obtain the pressure using Poisson's equation, the in-plane divergence of the pressure gradient is required:

$$\frac{\partial^2 p}{\partial x^2} + \frac{\partial^2 p}{\partial y^2} = -\rho\left[\frac{\partial}{\partial x}\left(\frac{Du}{Dt}\right) + \frac{\partial}{\partial y}\left(\frac{Du}{Dt}\right)\right] = -\rho f_{xy}. \tag{5}$$

The Poisson equation is then solved using a standard five-point scheme (second-order central differences):

$$\frac{p_{i+1,j} - 2p_{i,j} + p_{i-1,j}}{(\Delta x)^2} + \frac{p_{i,j+1} - 2p_{i,j} + p_{i,j-1}}{(\Delta y)^2} = -\rho f_{i,j}. \tag{6}$$

Boundary conditions are enforced on all edges of the pressure evaluation domain. These conditions comprise a reference boundary condition at a point or in a domain where pressure is prescribed, and Neumann conditions where the pressure gradient is prescribed on the remaining edges.

III. RESULTS AND DISCUSSION

Several previous investigations have considered the interactions of a spark-induced bubble with an elastic membrane; under jet impingement, the elastic membrane deforms rapidly and can even be pierced [11,12]. Herein, we report the occurrence of secondary cavitation around the deformed membrane with its movement, and we focus on the mechanism of cavitation induced by membrane deformation. In the following analysis, the collapse jet impacts the elastic membrane at time t_0.

In Sec. III A, we present a time series of representative images to compare the cases with and without secondary cavitation, and we provide the parameter range in which secondary cavitation occurs. In Sec. III B, we present the velocity and pressure fields during cavitation as obtained from the PIV experiment. In Sec. III C, we analyze how velocity and acceleration affect the occurrence of secondary cavitation, and we investigate the cavitation mechanism. Finally, in Sec. III D, we investigate the evolution of the cavitation bubble and the vortex flow induced by its collapse.

A. Cavitation caused by deformation of elastic membrane

For the cases with and without secondary cavitation, Fig. 4 shows the interactions between the spark-induced bubble and the membrane, as well as the subsequent induced secondary-cavitation dynamics.

For cavitation with $\gamma = 0.5$ and $d^* = 0.14$ as shown in Fig. 4(a), the spark-induced bubble expands rapidly to reach its maximum volume while the membrane is pushed gently downward at approximately $t_0 - 1260\,\mu\text{s}$. The bubble then contracts to form a mushroomlike shape, and the membrane rebounds upward at approximately $t_0 - 90\,\mu\text{s}$. Next, the bubble splits at its neck at approximately $t_0 - 30\,\mu\text{s}$ and creates two axial jets in opposite directions at approximately $t_0 - 20\,\mu\text{s}$. Subsequently, the elastic membrane deforms rapidly under the jet impingement at t_0. As the membrane continues to move downward, multiple tiny cavitation bubbles appear, covering the membrane surface in the lower flow field at approximately $t_0 + 80\,\mu\text{s}$. These secondary cavitation bubbles expand violently and merge into one substantial cavitation bubble at approximately $t_0 + 180\,\mu\text{s}$. Finally, the secondary cavitation bubble contracts and collapses along the membrane surface from approximately $t_0 + 650\,\mu\text{s}$ to $t_0 + 1170\,\mu\text{s}$.

For no cavitation with $\gamma = 0.6$ and $d^* = 0.14$ as shown in Fig. 4(b), under the weak impingement of the jet slowed down by the water layer and the gentle expansion of the split lower bubble, the membrane deforms gently from t_0 to $t_0 + 570\,\mu\text{s}$ compared to that in the case of cavitation; now, no cavitation occurs. Therefore, the occurrence of cavitation is assumed to be due to the significant effect of membrane deformation in the lower flow field. As shown in Fig. 5, the phase diagram for the occurrence of secondary cavitation was obtained by varying the dimensionless stiffness d^* of the membrane and the dimensionless standoff distance γ of the bubble from the membrane. Blue symbols indicate secondary cavitation, while red symbols indicate no secondary cavitation. For $d^* = 0.09$–0.23, the membrane can deform rapidly and substantially, thereby inducing secondary cavitation. By contrast, the absence of secondary cavitation has one of three causes, indicated by a triangle, a square, or a diamond. When indicated by a triangle, the membrane is pierced by the jet because of the membrane's thinness, as shown in Fig. 6(a). The remnant spark-induced bubble passes through the membrane and forms a piercing bubble, different from the secondary cavitation bubble; the piercing bubble expands and then collapses, a phenomenon also reported by Wang *et al.* [12]. When indicated by a square, the membrane deforms gently because of the large γ, which indicates that the strength of the jet impacting the membrane is weak, as shown in Fig. 6(b). When indicated by a diamond, the membrane again deforms gently but now because of the large d^*, which prevents significant membrane deformation under jet impact, as shown in Fig. 6(c). It suggested that d^* and γ have complex effects on the occurrence of secondary cavitation.

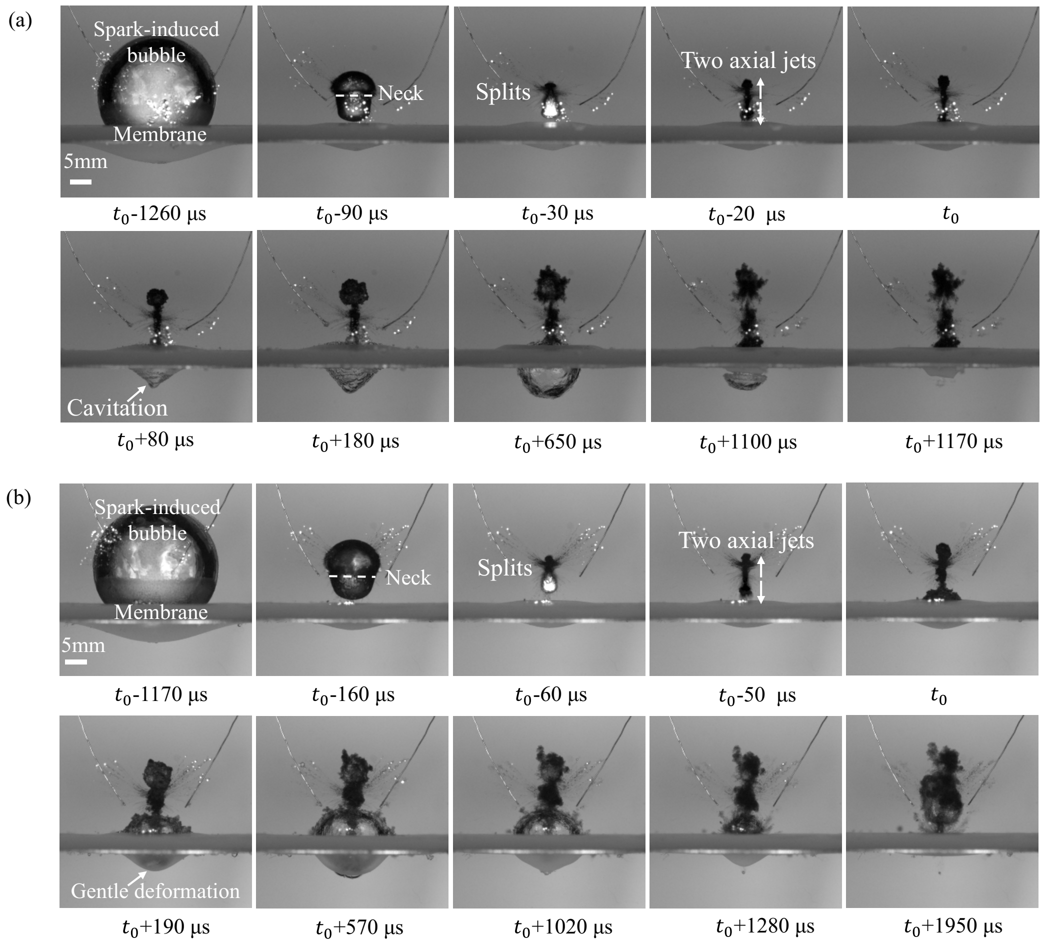

FIG. 4. Interactions of the spark-induced bubble and the elastic membrane: (a) cavitation occurrence ($\gamma = 0.5, d^* = 0.14$); (b) no cavitation occurrence ($\gamma = 0.6, d^* = 0.14$).

B. Time-resolved flow field caused by deformation of elastic membrane

To investigate the mechanism for cavitation, quantitative analysis of the flow field is necessary, and we obtained quantitative information about the flow field from the PIV experiment. Figure 7(a) ($\gamma = 0.5, d^* = 0.14$) shows the evolution of the velocity field below the elastic membrane just after the collapse jet impinges on the membrane. The velocity distribution along the membrane was extracted from the flow field, as shown in Fig. 8(a), with the y axis representing the horizontal direction. At $t = 0$, the lower flow field begins to accelerate because of the push from the membrane. The maximum velocity occurs consistently at the membrane apex, indicated by the red area in Fig. 7(a); this maximum velocity is oriented vertically, and the velocity distribution appears to be nonuniform. Specifically, the fluid velocity decreases rapidly along the tangential direction of the membrane from the apex, as evidenced by the transition from red to green [Fig. 7(a), $t_0 + 47$ μs]. Simultaneously, the velocity direction deviates from the vertical. In Fig. 8(a), the transition from a light-red curve to a dark-red curve shows the velocity evolution during the acceleration of the flow field from $t = 0$ to 60 μs, with the maximum velocity increasing from approximately 13 to 30 m/s. From 74 to 120 μs, the flow field decelerates. As shown in Fig. 7(a), the velocity near the membrane apex decreases rapidly compared to other areas of the flow field, depicted by the fading of red and

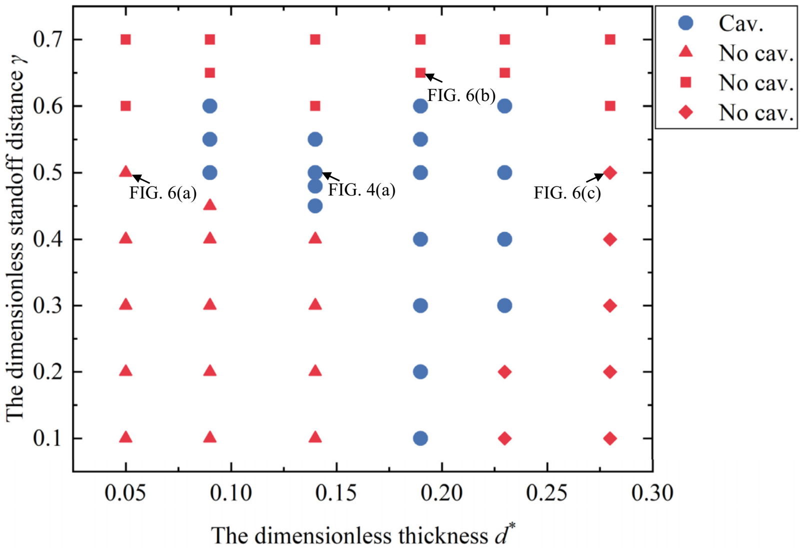

FIG. 5. Phase diagram for the occurrence of secondary cavitation with variation of the dimensionless elastic membrane stiffness $d^* = Ed/(\Delta pR_{\max})$ and standoff distance $\gamma = h/R_{\max}$. Blue symbols: cavitation (Cav.); red symbols: no cavitation (No cav.). Triangles: membrane is pierced; squares: membrane undergoes gentle deformation due to large γ; diamonds: membrane undergoes gentle deformation due to large d^*.

the transition to green. At 80 μs, cavitation occurs on both sides of the membrane apex, indicated by the gray ellipses. In Fig. 8(a), the transition from a dark-blue curve to a light-blue curve shows the deceleration process from 74 to 120 μs. The maximum velocity decreases from 30 to 15 m/s. At 80 μs, the velocity in the cavitation occurrence area is approximately 15–20 m/s indicated by black dotted lines.

Figures 7(b) and 8(b) show the velocity field with no cavitation and the extracted velocity distribution of the flow field along the membrane, respectively. From $t = 0$ to 80 μs, the flow field accelerates. The area of maximum velocity is also at the membrane apex, which changes from cyan blue at 0 μs to green at 80 μs without a significant velocity color-scale change as shown in Fig. 7(b). The maximum velocity increases slowly from 8 to 10 m/s, indicated by the velocity curves in Fig. 8(b). From 120 to 280 μs, the flow field decelerates. As shown in Fig. 7(b), the velocity field near the membrane apex transitions from green at 120 μs to light blue at 280 μs, and the velocity-field distribution becomes increasingly uniform. The maximum velocity decreases slowly from 10 to 5 m/s as shown in Fig. 8(b). No cavitation occurs during the deceleration process.

Comparing the velocity fields of the two cases shows the following. (1) The maximum velocity with cavitation is larger than that without cavitation. (2) The velocity distribution is less uniform with cavitation, with larger normal and tangential gradients in the flow field near the membrane apex. (3) The acceleration of the flow field is more drastic with cavitation, followed by a more drastic deceleration as well.

The pressure field was reconstructed from the velocity field. Figure 9 shows the evolution of the pressure field below the elastic membrane just after the collapse jet impacts the membrane, where the reference pressure is atmospheric pressure and is set to zero. The critical pressure for cavitation to occur is −98.7 kPa, which is the saturated vapor pressure at the reference pressure of zero. When cavitation occurs ($\gamma = 0.5, d^* = 0.14$) as shown in Fig. 7(a), the flow field is pushed by the membrane, and the highest pressure occurs near the membrane apex with a maximum value of approximately 800 kPa at $t = 0$. Subsequently, the pressure near the membrane apex decreases, indicated by the fading red. This is due to the weakening of the membrane's push on the flow field

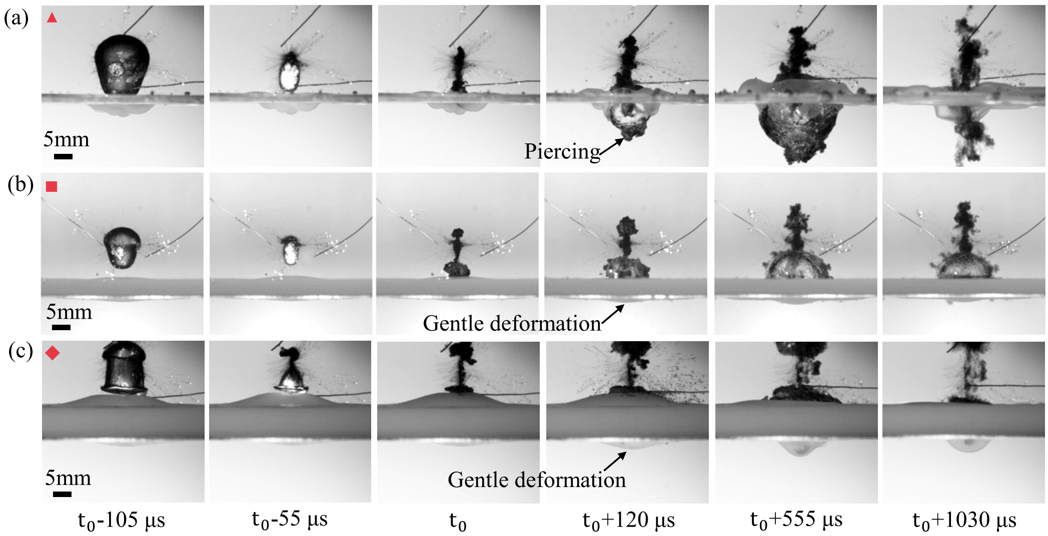

FIG. 6. No occurrence of secondary cavitation: (a) membrane is pierced by the jet, indicated by a triangle ($d^* = 0.05, \gamma = 0.5$); (b) membrane is deformed gently by the jet impact due to large γ, indicated by a square ($d^* = 0.19, \gamma = 0.65$); (c) membrane is deformed gently by the jet impact due to large d^*, indicated by a diamond ($d^* = 0.28, \gamma = 0.5$). In the Supplemental Material [41], see Video 1 of the secondary cavitation bubble and Video 2 of the piercing bubble.

because the impact force of the jet on the membrane decreases and the elastic resistance increases. At 74 µs, the pressure near the membrane apex begins to change from the highest pressure to the lowest. At 80 µs, the pressure near the membrane apex is below −98.7 kPa, and thus cavitation occurs. Then, such low pressure is maintained near the membrane that the secondary cavitation bubble expands violently.

For no cavitation ($\gamma = 0.6, d^* = 0.14$) as shown in Fig. 9(b), the highest pressure near the membrane apex is approximately 200 kPa at $t = 0$. The pressure near the membrane apex decreases gradually as the membrane pushes the flow field weakly. From 120 to 240 µs, the distribution of the pressure field is uniform, with the pressure being approximately 60 kPa. At 280 µs, the pressure near the membrane returns to around the reference pressure. In this case, the pressure is above or near the reference pressure, so no cavitation occurs.

Comparing the pressure fields of the two cases, the distribution of the pressure field in the case of cavitation is highly nonuniform, and the pressure change over time is much more significant compared to that without cavitation. The analysis of the flow field indicates that when cavitation occurs, the flow field exhibits greater variability over time, and the flow state undergoes more-pronounced changes. We hypothesize that the mechanism triggering cavitation can be attributed to either high velocity or the drastic change in the flow state.

C. Mechanism for cavitation

Based on the quantitative analysis of the flow field, the mechanism for cavitation is either high-speed flow or drastic changes in the flow state. In hydrodynamics, cavitation can be induced by high-speed flow along a projectile, where the static pressure drops below the saturated vapor pressure threshold. Also, cavitation can occur because of drastic changes in the flow state, leading to the inertia force of the fluid overcoming pressure differences.

First, the effect of velocity on the occurrence of secondary cavitation is investigated. Figure 10(a) shows the maximum tangential velocity along the membrane as a function of time. The blue

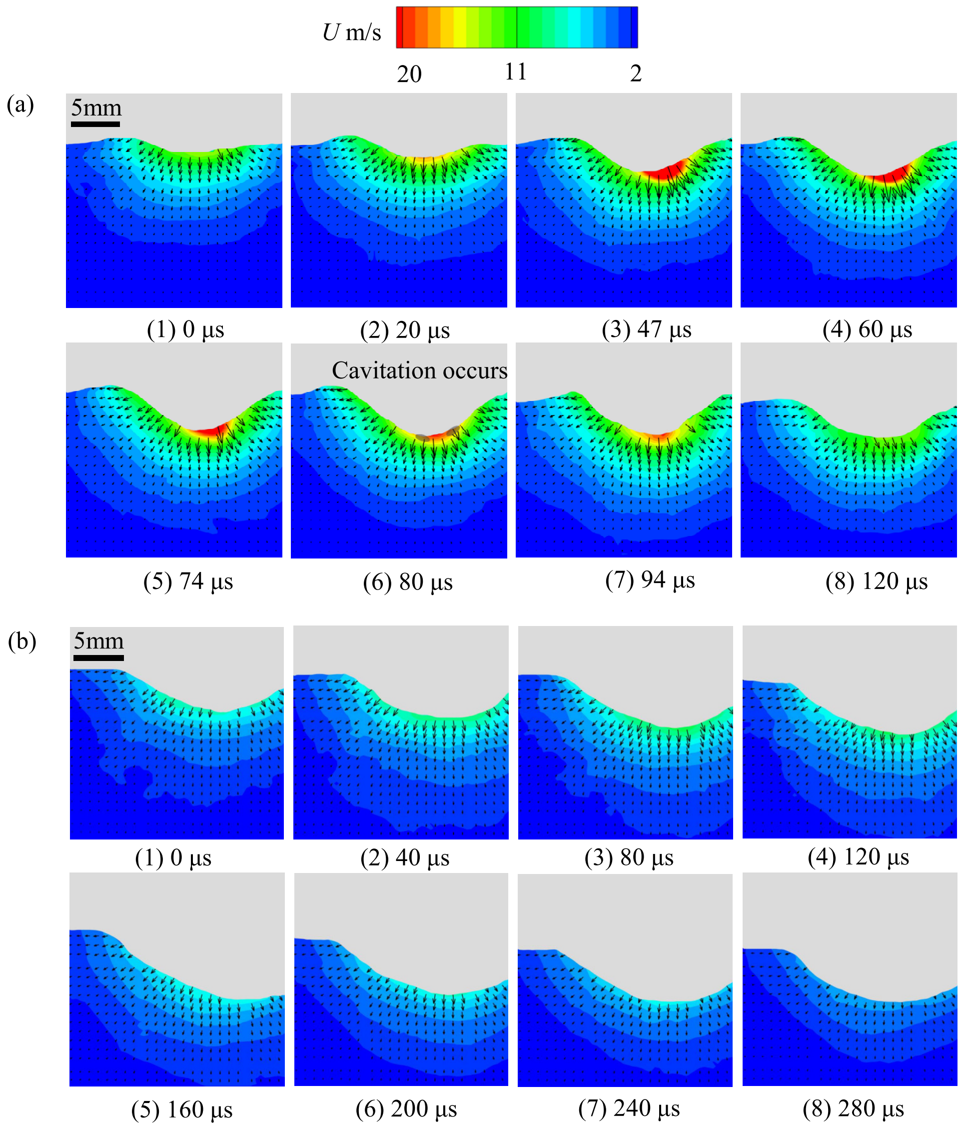

FIG. 7. Evolution of the velocity field below the elastic membrane just after the collapse jet impacts the membrane: (a) cavitation ($\gamma = 0.5, d^* = 0.14$; cavitation occurrences indicated by gray ellipses); (b) no cavitation ($\gamma = 0.6, d^* = 0.14$).

line indicates secondary cavitation for $d^* = 0.14$ and $\gamma = 0.5$, and the orange line indicates no cavitation for $d^* = 0.14$ and $\gamma = 0.6$. In both cases, the tangential velocity increases and then decreases. With secondary cavitation, the flow field near the membrane has positive pressure while reaching the maximum velocity, as shown in Fig. 10(b) for $t_0 + 20\,\mu\text{s}$ and $t_0 + 38\,\mu\text{s}$. Because the pressure is greater than the saturated vapor pressure, secondary cavitation does not occur. Therefore, we propose that velocity-induced pressure drop is not the primary mechanism for the occurrence of secondary cavitation.

In the classical context of high-speed flow surrounding a projectile, the velocity-based cavitation number $C = (p_a - p_v)/(0.5\rho U^2)$ is typically used to determine whether cavitation occurs. At a

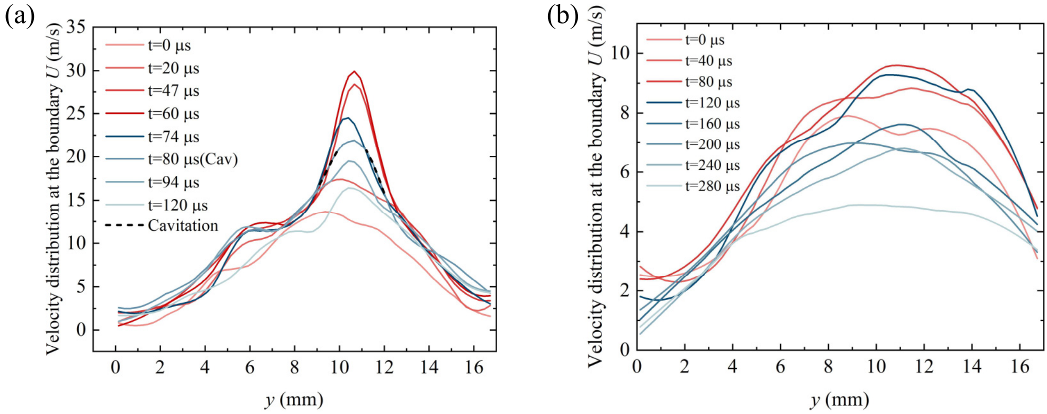

FIG. 8. Velocity distribution in the flow field near the elastic membrane, where the y axis is in the horizontal direction: (a) cavitation ($\gamma = 0.5$, $d^* = 0.14$; cavitation occurrence is indicated by black dotted lines); (b) no cavitation ($\gamma = 0.6$, $d^* = 0.14$). Red: acceleration phase; blue: deceleration phase.

velocity of 10 m/s ($C = 1.97$), a nonstreamlined body can undergo cavitation, while a streamlined body is not susceptible to cavitation [33–35]. The images of the membrane deforming [Fig. 4(a)] under jet impact indicate that the membrane exhibits a streamlined configuration and cavitation is unlikely to occur at the velocity equal to 10 m/s in our study. Next, the effect of acceleration on the occurrence of secondary cavitation is investigated. The dimensionless acceleration-induced inertial force a/g and the dimensionless pressure difference $\Delta p/(\rho g l)$ required to be overcome for cavitation are defined for analysis [36]. a is the characteristic acceleration of the flow field, defined as the vertical transient acceleration at the membrane apex. l is the characteristic length of the flow field, which represents the distance of the membrane apex motion from t_0 to a time t; we have $l = \sum_{t_0}^{t} u(t)dt$, where dt is the time interval. The time evolution of a/g and $\Delta p/(\rho g l)$ is shown in Fig. 11. As shown in Fig. 11(a), a/g exceeds $\Delta p/(\rho g l)$ during the deceleration phase where the occurrence of secondary cavitation is observed. As shown in Fig. 11(b), the inertial force is always lower than the pressure difference and secondary cavitation is not observed. It is therefore concluded that the primary mechanism responsible for the occurrence of secondary cavitation is the overcoming of the pressure difference by the acceleration-induced inertial force.

By examining the parameters $\Delta p/(\rho g l)$ and a/g, the regime of secondary cavitation is determined, as shown in Fig. 12.

a and l are expressed as the average acceleration and the distance traveled by the membrane apex during the deceleration phase, respectively. The blue symbols represent cases where secondary cavitation is observed, whereas the orange symbols represent cases without cavitation. Symbols of different shapes indicate membranes with different values of d^*. The occurrence of secondary cavitation is concentrated in the lower section of the diagonal in the majority of experimental cases. This suggests that secondary cavitation occurs when $\mathrm{Ca} = \frac{\Delta p}{\rho g l} / \frac{a}{g} < 1$.

D. Collapse of cavitation bubble and induced vortex flow

In this section, we delve deeper into the evolution of cavitation and the ensuing vortex flow induced by cavitation-bubble collapse and migration. Figure 13(a) provides a detailed view of the collapse of the secondary cavitation bubble. From 1140 to 1160 μs, the cavitation bubble contracts toward the membrane. When the cavitation bubble reaches its minimum volume at 1170 μs, a thin jet develops immediately toward the membrane. Thereafter, the remnant cavitation bubble initiates a second expansion. Subsequently, the remnant bubble detaches from the membrane and moves into the lower flow field, as shown in Fig. 13(b). Concurrently, the membrane rebounds. The remnant

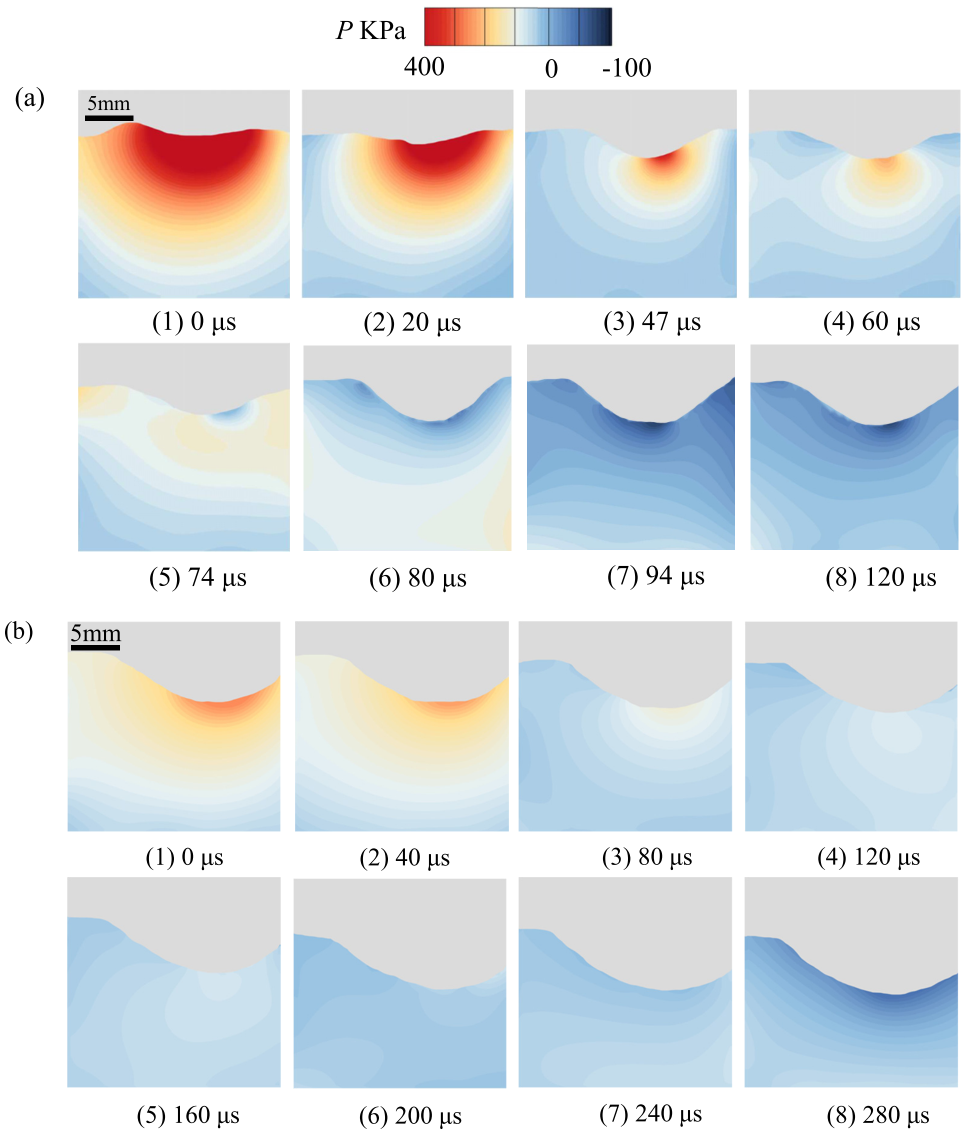

FIG. 9. Evolution of the pressure field below the elastic membrane just after the collapse jet impacts the membrane: (a) cavitation ($\gamma = 0.5$, $d^* = 0.14$); (b) no cavitation ($\gamma = 0.6$, $d^* = 0.14$).

cavitation bubble migrates away from the membrane as a cluster of bubbles rather than a single gas entity. During their downward migration, these bubbles oscillate in a coupled manner, dissipating the bubble energy and resulting in a gradual reduction in size of the remnant bubble.

In the PIV experiment, the velocity field during the evolution of the cavitation bubbles was obtained, as shown in Fig. 14(a) for $\gamma = 0.5$ and $d^* = 0.14$. The velocity at the lowest point of the cavitation-bubble contour was extracted to determine the cavitation-bubble growth rate, as shown in Fig. 14(b). In Fig. 14, the reference time of zero marks the onset of membrane deformation following impingement by the collapse jet. At 80 μs, cavitation initiates, commencing the first evolution cycle of the cavitation bubble. The initial expansion velocity of the cavitation bubble is approximately 20 m/s, denoted by the black point at 80 μs as shown in Fig. 14(b).The cavitation

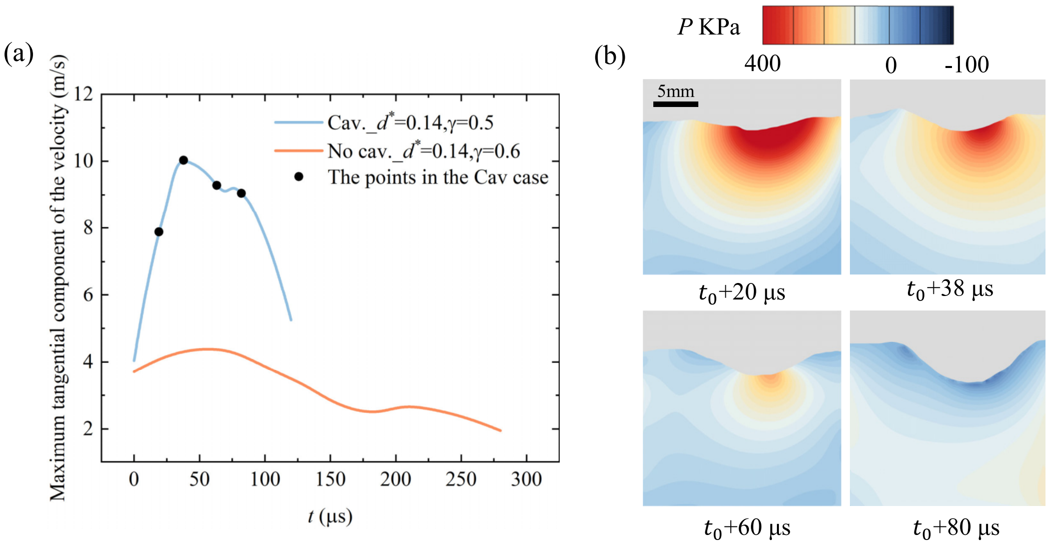

FIG. 10. (a) Maximum tangential velocity along the membrane as a function of time. Blue line: secondary cavitation ($d^* = 0.14$, $\gamma = 0.5$); orange line: no secondary cavitation ($d^* = 0.14$, $\gamma = 0.6$). (b) Pressure field corresponding to the black points in (a) for occurrence of secondary cavitation.

bubble expands with a decreasing velocity, reaching its maximum volume when the velocity becomes zero at 640 μs, as indicated by a black point. Subsequently, as the velocity at the lowest point of the contour turns negative, the cavitation bubble collapses at a gradually increasing velocity. It collapses to its minimum volume at 1147 μs, with a maximum collapse velocity of approximately −35 m/s, indicated by a black point. The remnant cavitation bubble then initiates the second cycle of evolution, expanding once again in the form of a bubble cluster, leading to a rapid reversal of fluid velocity near the lowest point of the contour. The maximum velocity of approximately 35 m/s is reached at 1187 μs, marked by a red point. We estimate the velocity of the thin jet by considering the velocity indicated by the red point, which is approximately 35 m/s. Additionally, we estimate

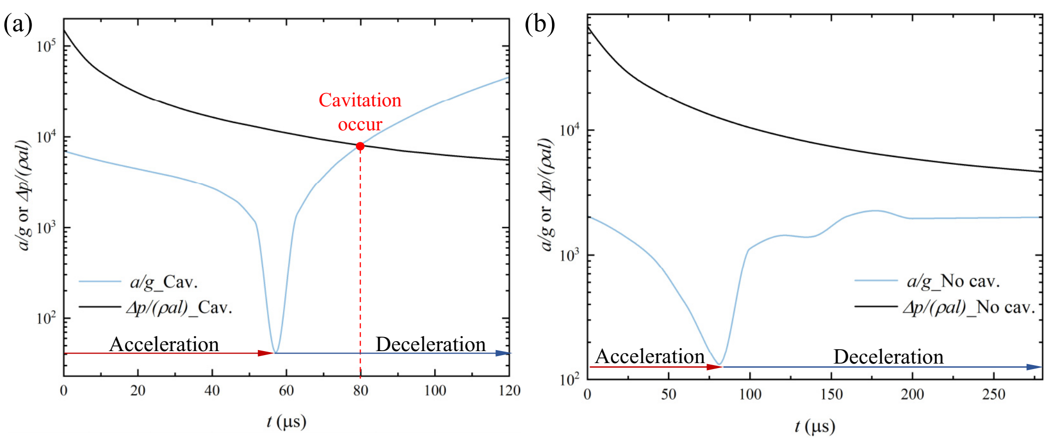

FIG. 11. Time evolutions of dimensionless acceleration-induced inertia force a/g and pressure difference $\Delta p/(\rho g l)$. (a) Secondary cavitation ($d^* = 0.14$, $\gamma = 0.5$). (b) No secondary cavitation ($d^* = 0.14$, $\gamma = 0.6$). Blue line: inertia force; black line: pressure difference.

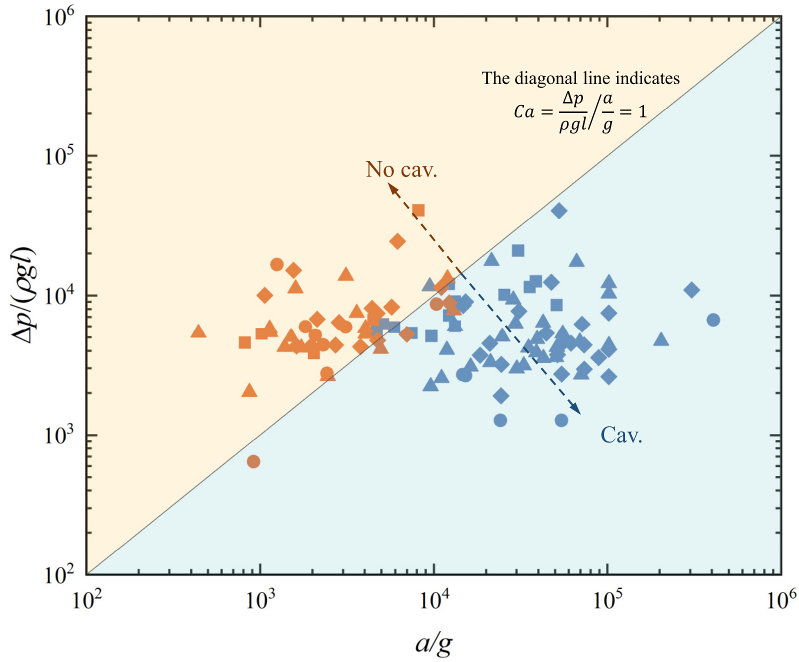

FIG. 12. Secondary cavitation regime depicted by $\Delta p/(\rho g l)$ and a/g. The diagonal line Ca $= \frac{\Delta p}{\rho g l} / \frac{a}{g} = 1$ is the dividing line between the occurrence and nonoccurrence of secondary cavitation. Blue symbols: secondary cavitation occurs; orange symbols: secondary cavitation does not occur. Symbols of different shapes indicate membranes with different values of d^* (circle: $d^* = 0.09$; square: $d^* = 0.14$; triangle: $d^* = 0.19$; diamond: $d^* = 0.23$).

the thin-jet velocity with different γ values ranging from 0.45 to 0.55 for $d^* = 0.14$, as shown in Fig. 14(c). The jet velocity tends to increase and then decrease with γ. We infer that the jet reaches its maximum velocity around $\gamma = 0.5$. The water hammer pressure of the jet impacting the membrane represents the potential force experienced by the membrane and serves as a valuable reference for biomedical applications.

Figure 15 shows the flow field when the remnant bubble detaches from the membrane and migrates downward. At $t = 1282\,\mu\text{s}$, a pair of vortex rings is generated (indicated by the white streamlines near the membrane) because of the annular flow. This annular flow is induced by the interaction between the flow toward the membrane caused by the contraction of the cavitation bubble in the first cycle and the flow away from the membrane caused by the rebound of the cavitation bubble in the second cycle. The vortex migrates downward at a velocity of approximately 3.9 m/s. Simultaneously, the membrane is also rebounding, causing the mainstream flow toward the membrane. At $1532\,\mu\text{s}$, the flow toward the membrane meets the downward flow caused by bubble migration, forming a circulation around the bubble, contributing to the development of the vortex. After the end of the membrane rebounds from $1781\,\mu\text{s}$, the flow field is mainly affected by the bubble downward migration with a velocity of approximately 1.5 m/s. By $4612\,\mu\text{s}$, the vortex center is moving toward the lower right at approximately 1.9 m/s. Subsequently, the right vortex core gradually moves beyond the recording range. By $7026\,\mu\text{s}$, only the left vortex core and part of the vortex center remain in the field of view with a downward velocity of approximately 2.5 m/s.

The Q criterion [37,38] is used to identify vortices and is one of the most popular vortex-identification methods. Q is a measure of the rotational magnitude over the shear magnitude: $Q > 0$ means that the rotational strength of the region is greater than the shear strength, so the rotational effect plays a dominant role and the region is defined as a vortex; $Q < 0$ means that

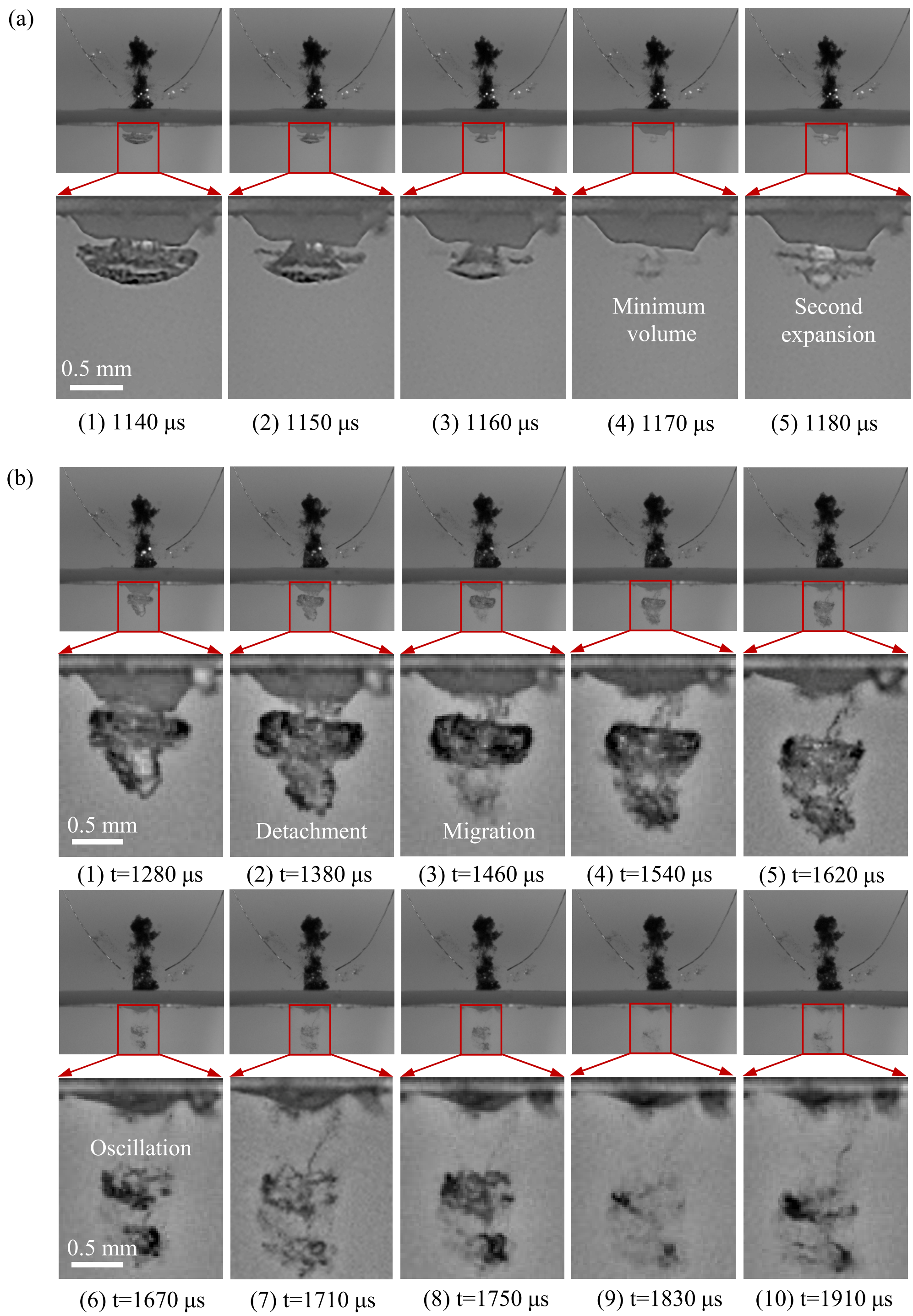

FIG. 13. (a) Details on the collapse of the secondary cavitation bubble for $\gamma = 0.5$, $d^* = 0.14$. (b) Imaging series of the remnant cavitation bubble detaching from the membrane, migrating downward, and oscillating for $\gamma = 0.5$, $d^* = 0.14$.

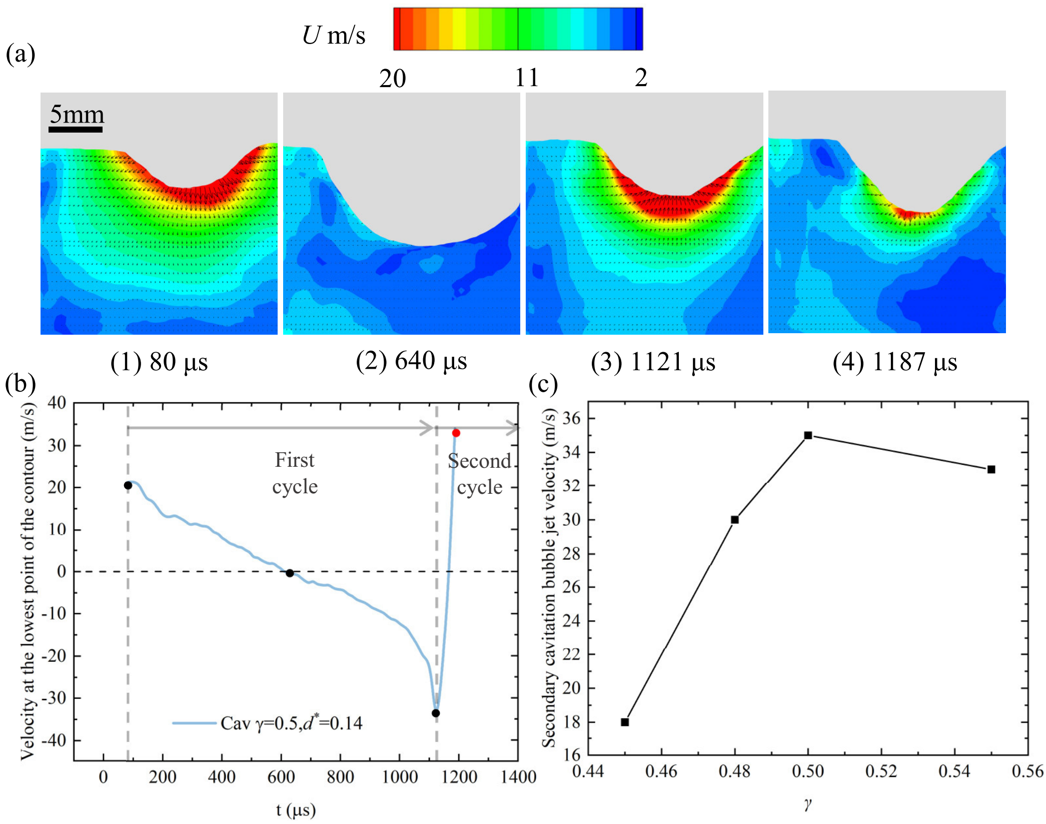

FIG. 14. (a) Flow field during the evolution of the cavitation bubble for $d^* = 0.14$, $\gamma = 0.5$. (b) Evolution of velocity at the lowest point of the cavitation-bubble contour for $d^* = 0.14$, $\gamma = 0.5$. The velocity fields in (a) correspond to the time points in (b). The velocity at the red point is estimated as the thin-jet velocity. (c) Estimated thin-jet velocity for $d^* = 0.14$ and $\gamma = 0.45, 0.48, 0.5, 0.55$.

the shear strength is greater than the rotational strength, and so the shear effect dominates. The Q distribution of the vortices generated by the collapse of the secondary cavitation bubble is shown in Fig. 16. At 1282 μs, the vortex pair (indicated by the red region) moves from the side to meet at the membrane apex. The rotation of the vortex leads to the shear effect (indicated by the blue region) gradually forming two distinct cores during rotation and downward migration from 1532 to 2114 μs. The vortex then moves to the lower-right corner, causing the red area of the right vortex core to gradually disappear. Finally, at 7026 μs, only the red region of the left vortex core remains in the image. By means of the Q criterion, the vortex structure is identified, and the vortex dynamics are analyzed preliminarily. The vortex flow induced by cavitation-bubble collapse is of great significance for engineering applications with mixing or transfer processes. It has been found that the collapse of a bubble near the solid wall can generate free vortices [39,40], which facilitate the enhancement of chemical reactions, mass transfer, and heat transfer, for example. Therefore, bubble-collapse-induced vortex flow near the elastic membrane deserves further investigation.

IV. CONCLUSION

We have observed secondary cavitation occurring during the rapid downward deformation of the membrane caused by the jet impingement. To investigate the mechanism for cavitation and its evolution characteristics, a diffuse-light experiment and a PIV experiment were performed. It was

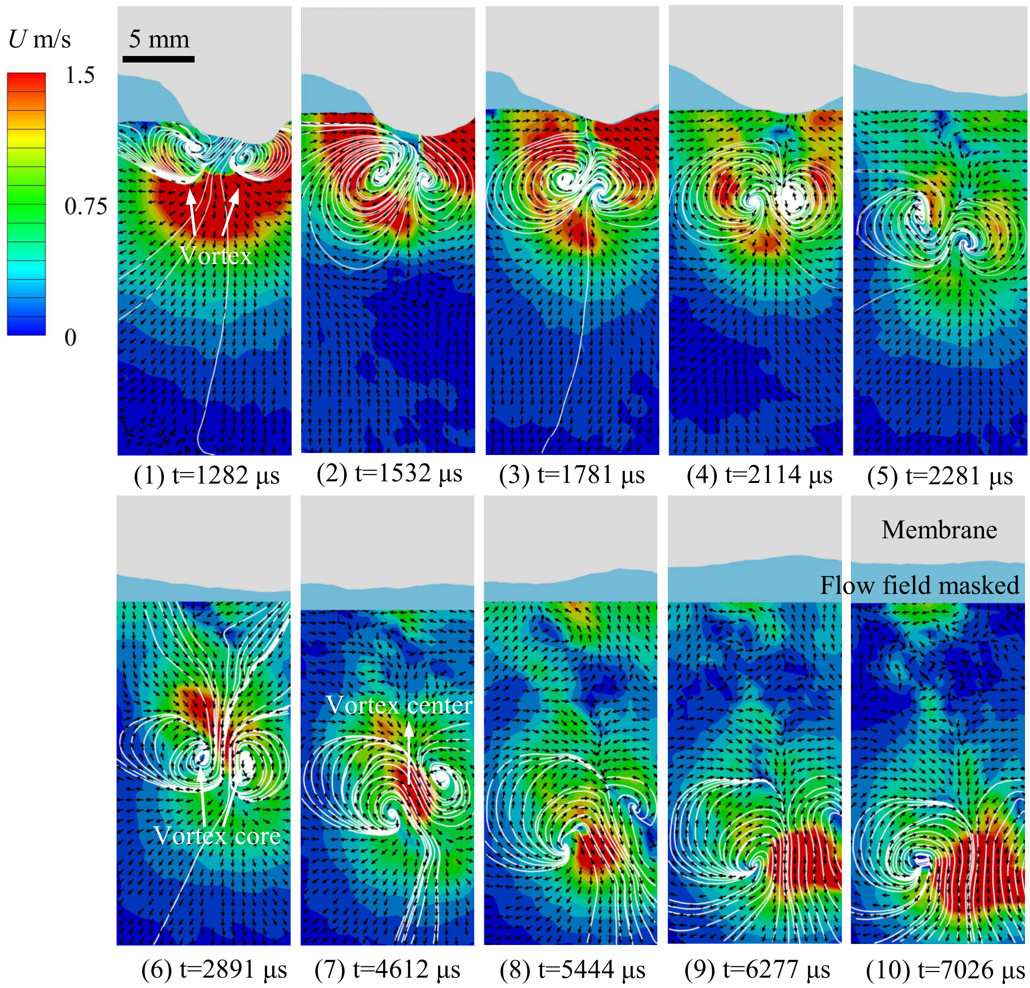

FIG. 15. Evolution of velocity field during the downward migration of the remnant bubble. Black arrows indicate the direction of the velocity vectors. Solid white lines indicate flow lines. The membrane is masked by the gray region, and part of the flow field is masked by the blue region. Bold white arrows indicate a pair of vortex rings in frame 1, vortex cores in frame 6, and a vortex center in frame 7.

found that secondary cavitation can occur when the dimensionless membrane stiffness d^* is in the range of 0.09–0.23.

By analyzing the velocity and pressure fields, the mechanism for cavitation was revealed. The membrane undergoes rapid and substantial deformation under the impingement of the collapse jet, and this movement of the membrane induces drastic acceleration and deceleration of the flow field. This drastic transition of the flow state leads to a substantial inertial effect in the fluid. Cavitation occurs when the inertial force overcomes the pressure difference. Through a parametric study of a/g and $\Delta p/(\rho g l)$, the regime of secondary cavitation was determined as $\mathrm{Ca} = \frac{\Delta p}{\rho g l} / \frac{a}{g} < 1$.

The evolution of secondary cavitation was studied, revealing that the thin jet of the cavitation bubble has an estimated velocity of approximately 35 m/s. This finding can serve as a reference for biomedical applications, where biological tissues may potentially be subjected to such jet impacts. Subsequently, a vortex is induced when the remnant bubble detaches from the membrane and migrates downward. The velocity of the vortex center is approximately 1.5–2 m/s. The rebound of

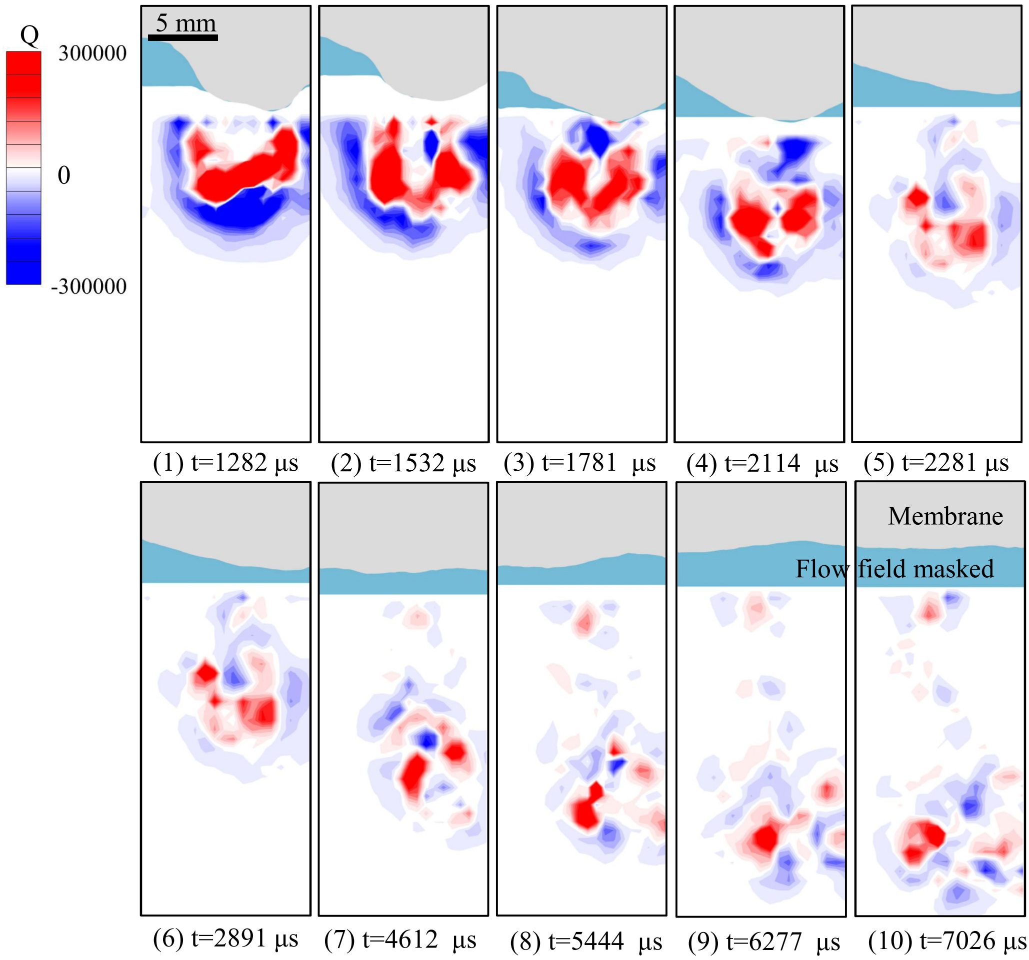

FIG. 16. Q distribution for vortex identification, corresponding to the velocity field in Fig. 15.

the elastic membrane may enhance the vortex strength and migration distance, resulting in increased mixing and faster transport. This aspect warrants further investigation for its potential benefits in various engineering applications.

ACKNOWLEDGMENTS

The authors gratefully acknowledge the group of Prof. Zhang at Harbin Engineering University for supplying the electric discharge machines and Dr. Li Hongyuan at Peking University for providing guidance on experimental measurements. This work was supported by the National Natural Science Foundation of China (Grants No. 12122214, No. 12272382, No. 12293000, No. 12293003, and No. 12293004), the Youth Innovation Promotion Association CAS (Grant No. 2022019), and the High-level Innovation Research Institute Program of Guangdong Province (Grants No. 2020B0909010003 and No. GARA2022002000).

APPENDIX A: DIMENSIONAL ANALYSIS

Dimensional analysis is conducted to investigate the correlation between the occurrence and nonoccurrence of secondary cavitation (δ) and the input parameters. Induced by the impact of the

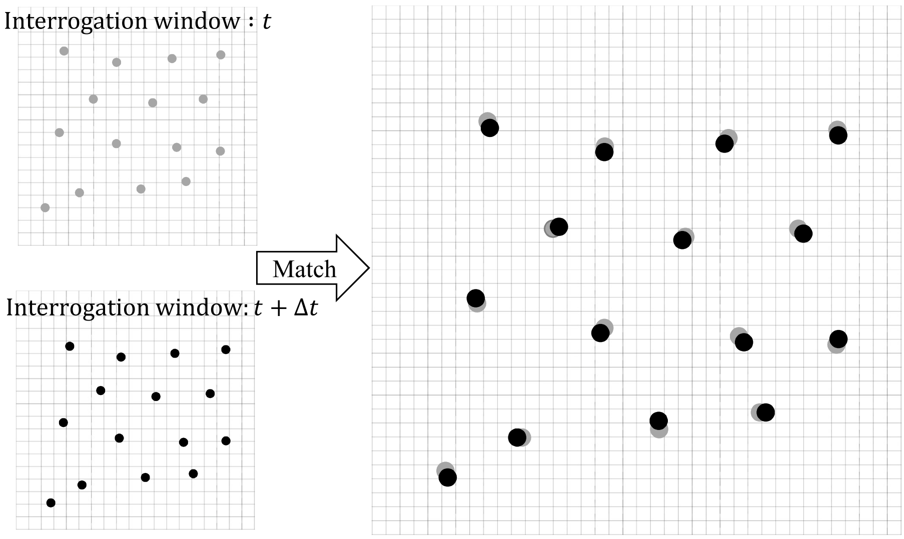

FIG. 17. Principle of PIV uncertainty quantification by correlation statistics. This method takes the corresponding interrogation windows at times t and $t + \Delta t$ to be matched through the computed displacement, considering individual pixels and their fluctuating contributions to the shape of the correlation peak.

collapse jet, the rapid deformation of the membrane leads to secondary cavitation. Under the current experimental conditions, the primary parameters considered are the maximum radius of the spark-induced bubble ($R_{\max}$), the distance between the center of the bubble and the membrane (h), the membrane elastic modulus (E), the membrane thickness (d), the ambient pressure (p_a), the saturated vapor pressure (p_v), and the fluid density (ρ). Consequently, the relationship between δ and the main parameters is obtained:

$$\delta = f(R_{\max}, h, E, d, p_a, p_v, \rho). \tag{A1}$$

The fundamental quantities $R_{\max}$, $\Delta p = p_a - p_v$, and ρ are selected to make Eq. (A1) dimensionless:

$$\delta = f\left(\frac{Ed}{\Delta p R_{\max}}, \frac{h}{R_{\max}}\right) = f(d^*, \gamma). \tag{A2}$$

As reported by Pan *et al.* [36], acceleration-induced cavitation can be discriminated by Ca, yielding the relationship $\mathrm{Ca} = f'(\frac{Ed}{\Delta p R_{\max}}, \frac{h}{R_{\max}}) = f'(d^*, \gamma)$.

APPENDIX B: DETAILS OF PIV UNCERTAINTY EVALUATION

The uncertainty in PIV measurements is evaluated using correlation statistics [30]. This method considers individual pixels and their fluctuating contributions to the shape of the correlation peak from which an uncertainty estimate is derived. The following equations are provided for the u component in the x direction, but they apply equally to the v component in the y direction.

The principle of the correlation-statistics method is shown schematically in Fig. 17. It shows two corresponding interrogation windows: the first one for the moment t and the second one for the moment $t + \Delta t$. The window for $t + \Delta t$ can be dewarped back onto the window for t using the displacement field u. An interrogation window consists of $N = n \times n$ pixels with n pixels in each dimension, denoting each pixel with i. For each pixel, the intensity at moment t is $I_1(x)$, and the intensity at moment $t + \Delta t$ is

$$I_2^* = I_2(x + u). \tag{B1}$$

The correlation function for each pixel is

$$c(u) = I_1(x, y)I_2(x + u, y) = I_1(x, y)I_2^*(x, y). \tag{B2}$$

A small distance $\pm\Delta x$ away from u, the correlation function c_+, denoted as $c(u + \Delta x)$, should therefore be equal to c_-, denoted as $c(u - \Delta x)$:

$$\Delta c = c_+ - c_- = I_1(x, y)I_2^*(x + \Delta x, y) - I_1(x, y)I_2^*(x - \Delta x, y) \cong 0. \tag{B3}$$

An interrogation window considers the effects of all pixels therein. Thus, within an interrogation window we have $C = \sum_i^N c_i$, $C_+ = \sum_i^N c_{+i}$, and $C_- = \sum_i^N c_{-i}$. Considering the three points $C_0 = C(u)$, C_+, and C_- allows for the calculation of an improved optimal displacement $u + \delta u$. Fitting a Gaussian curve through these three points enables the determination of the residual displacement δu, given by

$$\delta u = \frac{\Delta x}{2} \frac{\log_{10}(C_+) + \log_{10}(C_-)}{2\log_{10}(C_0) - \log_{10}(C_+) - \log_{10}(C_-)} = f(C_0, C_+, C_-) = f\left(C_0, C_\pm - \frac{\Delta C}{2}, C_\pm + \frac{\Delta C}{2}\right), \tag{B4}$$

where $C_\pm = (C_+ + C_-)/2$. Every term Δc_i represents the elemental contribution to the total correlation difference ΔC:

$$\Delta C = \sum_i^N \Delta c_i. \tag{B5}$$

Because of various error sources, the two windows will not match perfectly. This difference is optimized away by the PIV predictor–corrector scheme such that ΔC is zero again, leading to an erroneously measured displacement $u' = u + \delta u$. Thus, from the given known variability in Δc_i, an estimate of the standard deviation $\sigma_{\Delta C}$ of ΔC can be derived, which is then propagated by Eq. (B4) to an uncertainty estimate of the displacement field.

In general, the standard deviation of ΔC is related to the sum of the covariance matrix of Δc_i:

$$\sigma_{\Delta C}^2 \equiv \text{var}\left(\sum_i^N \Delta c_i\right) = \sum_{i,j}^N (\text{cov}(\Delta c_i, \Delta c_j)). \tag{B6}$$

Finally, using Eq. (B4), the uncertainty estimation of the displacement field can be computed as

$$\sigma_u = f\left(C_0, C_\pm - \frac{\sigma_{\Delta C}}{2}, C_\pm + \frac{\sigma_{\Delta C}}{2}\right). \tag{B7}$$

---

[1] K. Kooiman, S. Roovers, S. A. G. Langeveld, R. T. Kleven, H. Dewitte, M. A. O'Reilly, J. M. Escoffre, A. Bouakaz, M. D. Verweij, K. Hynynen, I. Lentacker, E. Stride, and C. K. Holland, Ultrasound-responsive cavitation nuclei for therapy and drug delivery, Ultrasound Med. Biol. **46**, 1296 (2020).

[2] K. R. Rau, P. A. Quinto-Su, A. N. Hellman, and V. Venugopalan, Pulsed laser microbeam-induced cell lysis: Time-resolved imaging and analysis of hydrodynamic effects, Biophys. J. **91**, 317 (2006).

[3] S. L. Zhu, F. H. Cocks, G. M. Preminger, and P. Zhong, The role of stress waves and cavitation in stone comminution in shock wave lithotripsy, Ultrasound Med. Biol. **28**, 661 (2002).

[4] C. K. Turangan, G. P. Ong, E. Klaseboer, and B. C. Khoo, Experimental and numerical study of transient bubble-elastic membrane interaction, J. Appl. Phys. **100**, 054910 (2006).

[5] A. H. Aghdam, V. Farhangmehr, S. W. Ohl, B. C. Khoo, and M. T. Shervani-Tabar, Characterization of the interaction of two oscillating bubbles near a thin elastic membrane, Exp. Fluids **53**, 1723 (2012).

[6] U. Orthaber, R. Petkovsek, J. Schille, L. Hartwig, G. Hawlina, B. Drnovsek-Olup, A. Vrecko, and I. Poberaj, Effect of laser-induced cavitation bubble on a thin elastic membrane, Opt. Laser Technol. **64**, 94 (2014).

[7] Z. Lokar, R. Petkovsek, and M. Dular, Cavitation bubble dynamics in a vicinity of a thin membrane wetted by different fluids, Sci. Rep. **11**, 3506 (2021).

[8] A. B. Sieber, D. B. Preso, and M. Farhat, Cavitation bubble dynamics and microjet atomization near tissue-mimicking materials, Phys. Fluids **35**, 027101 (2023).

[9] Q. D. Yu, Z. C. Xu, J. Zhao, M. D. Zhang, and X. J. Ma, PIV-based acoustic pressure measurements of a single bubble near the elastic boundary, Micromachines **11**, 637 (2020).

[10] S. R. Gonzalez-Avila, A. C. van Blokland, Q. Zeng, and C.-D. Ohl, Jetting and shear stress enhancement from cavitation bubbles collapsing in a narrow gap, J. Fluid Mech. **884**, A23 (2020).

[11] X. Y. Kan, J. L. Yan, S. Li, and A. M. Zhang, Rupture of a rubber sheet by a cavitation bubble: An experimental study, Acta Mech. Sin. **37**, 1489 (2021).

[12] A. Wang, Y. X. Zhong, G. H. Wang, J. Huang, J. Z. Wang, and Y. W. Wang, Experimental study on the formation of two axial jets of cavitation bubbles near soft membranes with different thicknesses, AIP Adv. **12**, 095023 (2022).

[13] J. Z. Wang, G. Wang, Q. Y. Zeng, and Y. W. Wang, Recent progress on the jetting of single deformed cavitation bubbles near boundaries, J. Hydrodyn. **35**, 832 (2023).

[14] E. A. Brujan, K. Nahen, P. Schmidt, and A. Vogel, Dynamics of laser-induced cavitation bubbles near an elastic boundary, J. Fluid Mech. **433**, 251 (2001).

[15] E. A. Brujan, K. Nahen, P. Schmidt, and A. Vogel, Dynamics of laser-induced cavitation bubbles near elastic boundaries: Influence of the elastic modulus, J. Fluid Mech. **433**, 283 (2001).

[16] W. L. Xu, Y. W. Zhai, J. Luo, Q. Zhang, and J. B. Li, Experimental study of the influence of flexible boundaries with different elastic moduli on cavitation bubbles, Exp. Therm. Fluid Sci. **109**, 109897 (2019).

[17] J. Mur, V. Agrez, J. Petelin, and R. Petkovsek, Microbubble dynamics and jetting near tissue-phantom biointerfaces, Biomed. Opt. Express **13**, 1061 (2022).

[18] Y. W. Zhai, W. L. Xu, J. Luo, and J. B. Li, Experimental study on the characteristics of microjets and shock waves of cavitation bubbles near elastic boundaries, Ocean Eng. **257**, 111664 (2022).

[19] O. Supponen, D. Obreschkow, P. Kobel, M. Tinguely, N. Dorsaz, and M. Farhat, Shock waves from nonspherical cavitation bubbles, Phys. Rev. Fluids **2**, 093601 (2017).

[20] D. Obreschkow, P. Kobel, N. Dorsaz, A. de Bosset, C. Nicollier, and M. Farhat, Cavitation bubble dynamics inside liquid drops in microgravity, Phys. Rev. Lett. **97**, 094502 (2006).

[21] O. Lindau and W. Lauterborn, Cinematographic observation of the collapse and rebound of a laser-produced cavitation bubble near a wall, J. Fluid Mech. **479**, 327 (2003).

[22] P. Robinson, J. Blake, T. Kodama, A. Shima, and Y. Tomita, Interaction of cavitation bubbles with a free surface, J. Appl. Phys. **89**, 8225 (2001).

[23] Y. Tomita, T. Kodama, and A. Shima, Secondary cavitation due to interaction of a collapsing bubble with a rising free-surface, Appl. Phys. Lett. **59**, 274 (1991).

[24] J. Z. Wang, G. H. Wang, and Y. W. Wang, Splashing and sealing of an ejecta sheet induced by a cavitation bubble close to a water surface, Phys. Fluids **36**, 043312 (2024).

[25] C. E. Brennen, *Hydrodynamics of Pumps* (Oxford University Press, Oxford, 1994).

[26] W. Lauterborn, T. Kurz, R. Mettin, and C. D. Ohl, Experimental and theoretical bubble dynamics, in *Advances in Chemical Physics*, edited by I. Prigogine and S. A. Rice (Wiley, Hoboken, 1999), Vol. 110, pp. 295–380.

[27] J. Daily, J. Pendlebury, K. Langley, R. Hurd, S. Thomson, and T. Truscott, Catastrophic cracking courtesy of quiescent cavitation, Phys. Fluids **26**, 091107 (2014).

[28] A. Kiyama, Y. Tagawa, K. Ando, and M. Kameda, Effects of a water hammer and cavitation on jet formation in a test tube, J. Fluid Mech. **787**, 224 (2016).

[29] X. W. Luo, B. Ji, and Y. Tsujimoto, A review of cavitation in hydraulic machinery, J. Hydrodyn. **28**, 335 (2016).

[30] B. Wieneke, PIV uncertainty quantification from correlation statistics, Meas. Sci. Technol. **26**, 074002 (2015).
[31] R. de Kat and B. W. Van Oudheusden, Instantaneous planar pressure determination from PIV in turbulent flow, Exp. Fluids **52**, 1089 (2012).
[32] B. W. Van Oudheusden, PIV-based pressure measurement, Meas. Sci. Technol. **24**, 032001 (2013).
[33] J. Katz, Cavitation phenomena within regions of flow separation, J. Fluid Mech. **140**, 397 (1984).
[34] V. Arakeri and V. Ramarajan, Inception of cavitation from a backward facing step, J. Fluids Eng. **103**, 288 (1981).
[35] R. E. A. Arndt, Cavitation in fluid machinery and hydraulic structures, Annu. Rev. Fluid Mech. **13**, 273 (1981).
[36] Z. Pan, A. Kiyama, Y. Tagawa, D. J. Daily, S. L. Thomson, R. Hurd, and T. T. Truscott, Cavitation onset caused by acceleration, Proc. Natl. Acad. Sci. USA **114**, 8470 (2017).
[37] J. Hunt, A. Wray, and P. Moin, Eddies, streams, and convergence zones in turbulent flows, *Center for Turbulence Research, Proceedings of the 1988 Summer Program* (NASA, 1988).
[38] F. Jeong and J. Hussain, On the identification of a vortex, J. Fluid Mech. **285**, 69 (1995).
[39] F. Reuter, S. R. Gonzalez-Avila, R. Mettin, and C. -D. Ohl, Flow fields and vortex dynamics of bubbles collapsing near a solid boundary, Phys. Rev. Fluids **2**, 064202 (2017).
[40] J. L. Huang, J. Z. Wang, J. Huang, P. Y. Lv, H. Y. Li, and Y. W. Wang, Effects of wall wettability on vortex flows induced by collapses of cavitation bubbles: A numerical study, Phys. Fluids **35**, 087122 (2023).
[41] See Supplemental Material at http://link.aps.org/supplemental/10.1103/PhysRevFluids.9.093604 for the secondary cavitation bubble and the piercing bubble.